RSC Advances

ROYAL SOCIETY OF CHEMISTRY

www.rsc.org/advances

Journal Name

ARTICLE

Controlled synthesis and morphology dependent luminescence of $Lu_2O_2S:Eu^{3+}$ phosphors

Received 00th January 20xx,
Accepted 00th January 20xx

DOI: 10.1039/x0xx00000x

www.rsc.org/

Bowen Zhang, Haifeng Zou，Yunzhi Dai，Yanhua Song， Keyan Zheng，Xiuqing Zhou and Ye Sheng[a]

$Lu_2O_2S:Eu^{3+}$ phosphors were successfully prepared with controllable morphology, including 3D sphere-like, cloud-like, nested tetrahedron, flower-like and 1D rod-like architectures. It is indicated that pH value of the system plays an important role in the morphology and the degree of crystallinity of the product. Interestingly, with morphological changes, the band gap energy of Lu_2O_2S crystal changed, followed by a variation of the crystal field symmetry and further the luminescence performance. Therefore, such a morphology-sensitive luminescence property was first interpreted in terms of degree of crystallinity, band gap energy, and the crystal field symmetry around Eu^{3+}.

Introduction

Inorganic phosphors are widely applied in the field of light emitting displays, optoelectronics, lasers, and as fluorescent markers in biomedicine[1-4]. The luminescence properties of these materials are strongly dependent on their chemical compositions, phases, dimensions, and most importantly their morphologies[5-7]. As a consequence, much effort has been devoted to fabricating inorganic luminescent materials with specific morphologies, such as wires, rods, sheets, cubes, hollow spheres, and flowers[8, 9]. In spite of great progress in preparing inorganic luminescent materials of various types of morphologies, it is still a challenge to comprehend the nature of the impact of morphology on the luminescent properties[10, 11].

Rare-earth doped oxysulfides M_2O_2S (M = Y, La-Lu) are attractive materials and have received much intense research interests due to their potential applications in high-performance luminescent devices, catalysts, and other functional materials and so forth[12-14]. However, the oxysulfide family is delicate to synthesize because of lack of affinity between the Ln^{3+} (Ln = La-Lu) and the S^{2-} [15]. Therefore, much effort has been directed toward the synthesis of micro/nano-scale and shape-controllable lanthanide chalcogenides[16-18]. Song prepared uniform $Gd_2O_2S:Ln^{3+}$ (Ln = Eu, Tb) submicrospheres through solvothermal method followed by a heat treatment[19]; Yan synthesized ultrathin Ln_2O_2S (Ln = La-Tb, Y) nanoplates using Na^+ and Li^+ ions as dopants in oleic acid/oleylamine/1-octadecene mixed solvent[20]; Qi studied the synthesis and luminescence properties of 3D-hierarchical $Lu_2O_2S:Eu^{3+}$ micro/nano-structures[21]. Our group has reported the preparation and luminescence properties of novel 3D $Lu_2O_2S:Eu^{3+}$ microstructure[22] and 1D $Lu_2O_2S:Eu^{3+}$ nanorods[23]. However, the synthesis of rare earth oxysulfide with controllable dimensionality and tunable shapes[24] still remains a challenge, and knowledge about structure pertinent to the luminescence property is still rather poor[25-27].

Herein, we reported on the morphology-controllable synthesis of $Lu_2O_2S:Eu^{3+}$ via a hydrothermal method followed by a subsequent calcination process. By simply changing the pH values of the reaction mixture, $Lu_2O_2S:Eu^{3+}$ precursors were successfully prepared to show various morphologies, including 3D sphere-like, cloud-like, nested tetrahedron, flower-like and 1D rod-like, and the as-formed precursors could be transformed into $Lu_2O_2S:Eu^{3+}$ with their original morphologies maintained. The possible mechanisms for the growth processes into diverse morphologies were analyzed. Furthermore, the dependence of $Lu_2O_2S:Eu^{3+}$ luminescence performance on different morphologies has been explored and the possible reasons are proposed. It is anticipated that the findings reported here may help in obtaining an insight into the morphology-dependent red luminescence.

Experimental

The rare-earth oxides RE_2O_3 (RE = Lu, Eu) (99.99%) were purchased from Tianjin Chemical Reagent Co. $Lu(NO_3)_3$ and $Eu(NO_3)_3$ were prepared by dissolving the corresponding metal oxide in nitric acid at elevated temperatures. The other chemicals were bought from Sinopharm Group Co. Ltd. All reagents were analytical grade and were used without further purification in the experiment.

Synthesis of $Lu_2O_2S:Eu^{3+}$ nanostructures

In a typical procedure, 1.95 mL of $Lu(NO_3)_3$ (1 M) and 1 mL of $Eu(NO_3)_3$ (0.05 M) were added into 25 mL of ethylene glycol (EG) first, then 2.0 g of polyvinylpyrrolidone (PVP K30, M ¼ 40,000) were thoroughly dissolved in the mixture with vigorous agitation. Afterwards, 10 mL of ethanol solution containing 0.11 g of thiourea

[a] College of chemistry, Jilin University, Changchun 130012, P. R. China, E-mail: shengye@jlu.edu.cn

($SC(NH_2)_2$) was added dropwise into the above solution. Subsequently, sodium hydroxide solution (2 M) was introduced dropwise to adjust the pH value. After additional agitation for 30 min, the feedstock was transferred to a 100 mL Teflon-lined stainless autoclave and heated at 200 ℃ for 24 h. When the autoclave was cooled to room-temperature naturally, the precipitate was collected by centrifugation, washed with ethanol and deionized water thrice respectively, and dried at 60 ℃ overnight in air. The final products were obtained by calcinations of precursors at 600 ℃ for 2 h under an inert N_2/S atmosphere. The heating rate is 1 ℃ min^{-1}.

Characterization

The samples were characterized by powder X-ray diffraction (XRD) performed on a XRD-6000 X-ray diffractometer (Shimadzu) with Cu Kα radiation (k = 0.154056 nm). The size and morphology of the samples were inspected by a field emission scanning electron microscope equipped with an energy-dispersive spectroscopy (EDS) (FE-SEM, S-4800, and Hitachi, Japan). The photoluminescence (PL) excitation and emission spectra were recorded with a Jobin Yvon FluoroMax-4 equipped with a 150 W xenon lamp as the excitation source under a working voltage of 700 V. All the measurements of PL emission spectra were performed with excitation wavelength at 270 nm at room temperature. (atmosphere: air, excitation-slit/detection-slit: 3 nm/3 nm, measure time: 0.1 s, step width: 1.0 nm, the thickness of the phosphor layers: 0.2 mm.) Luminescence lifetime measurements were determined on an Edinburgh Instrument FLS920 phosphor meter using a 450W xenon lamp as the excitation source (pulse width, 3 μs). UV–vis diffuse reflectance spectra of the samples were measured on a U-4100 UV–vis–NIR spectrophotometer with $BaSO_4$ as the background. All the measurements were performed at room temperature.

Results and discussion

Morphological analysis

The morphologies of the samples were controlled by varying the pH value of the reaction system. As indicated by the SEM image of Fig. 1A, the solvothermal precursors obtained at pH = 5.0 consist of separated spheres with diameter of 230-240 nm. When the pH value is adjusted to 7.0, the precursors are composed of some cloud-like particles (Fig. 1B), with a rough surface, showing apparent boundaries between the constituent particles. Like the precursors obtained at pH = 5.0, those precursors obtained at pH = 9.0 (Fig. 1C) are also separated spheres, but their diameters are decreased to 100-110 nm. Fig. 1D indicated that the precursors obtained at pH = 12.0 consist of many uniform and monodisperse microstructures, which are composed of two intertwined tetrahedrons, slotted into each other. As shown in Fig. 1E, when the pH value was moderately increased to 12.5, microflowers were obtained. It can be seen that the microflowers are composed of a bundle of outspread nanorods, which are closely bonded to each other in the middle. On increasing the pH value to 13.0, some uniform nanorods were obtained with dimensions of 20-40 nm in diameter and 400-600 nm in length, as shown in Fig. 1F.

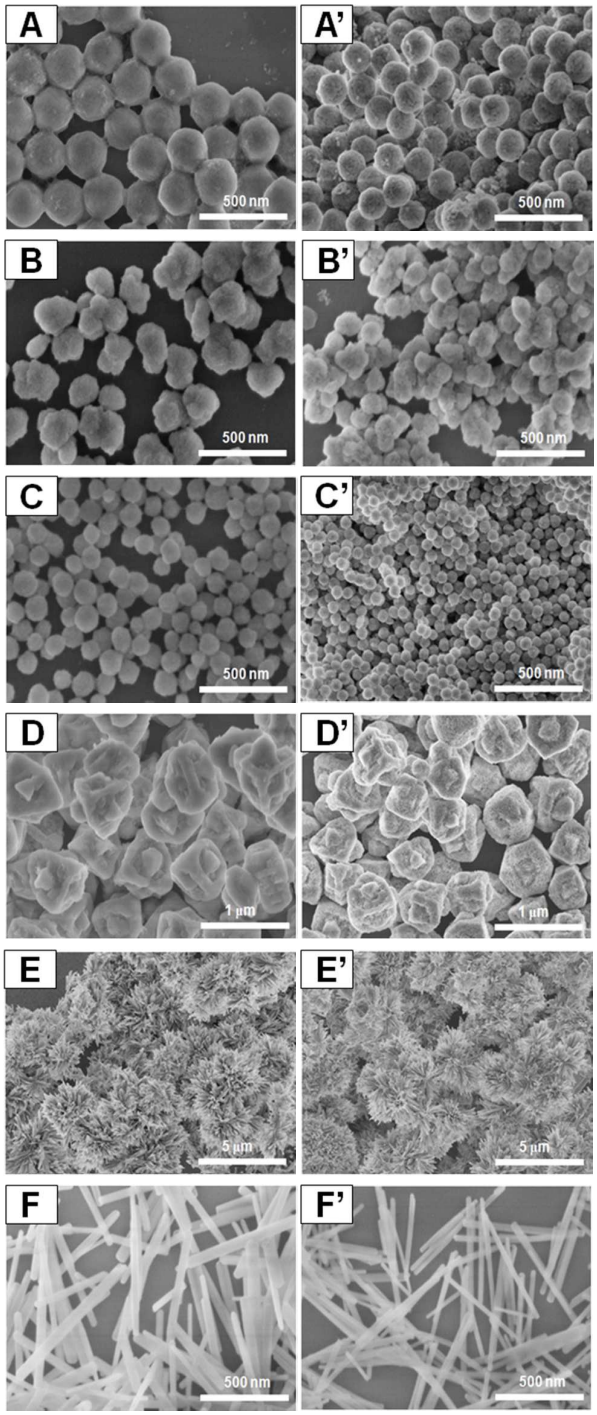

Fig. 1 SEM images of lutetium oxysulfide precursors obtained at different pH values and their corresponding annealed products: 5.0 (A and A'), 7.0 (B and B'), 9.0 (C and C'), 12.0 (D and D'), 12.5 (E and E'), 13.0 (F and F').

Fig. 1A', 1B', 1C', 1D', 1E' and 1F' are the SEM images of the corresponding annealed products. It was shown that the precursors' morphologies have not been changed after they were annealed at 600 ℃ for 2 h and six kinds of morphologies of $Lu_2O_2S:Eu^{3+}$ (as proved by XRD and EDS) have been obtained; they are sphere-like (160-170 nm), cloud-like, sphere-like (60-70 nm), nested

tetrahedron, flower-like and rod-like. The fact that the obtained $Lu_2O_2S:Eu^{3+}$ products all inherit the morphologies of the precursors is attributed to the higher activation energies needed for the collapse of these structures. At the same time, it can be noted that the annealed samples were shrinked compared with the precursors, which may be due to the decomposition of the organic compound in the precursors and the release of some gases (H_2O, NO_2, etc.) during the calcination process.

Structural analysis

Fig. 2 shows the XRD patterns of the precursors obtained at different pH values as well as the JCPDS cards No. 79-1352 and No. 26-1445. There is only one broad peak near 2θ = 28.55 in the curve of the precursors that obtained at pH = 5.0 and pH = 7.0, indicating that the two precursors are amorphous compounds. Although the XRD pattern of the precursors which obtained at pH = 9.0 and pH = 12.0 indicated a good crystalline phase, their crystal structures could not be indexed to any known lutetium compounds. However, the major diffraction peaks of the two samples can be indexed to monoclinic phase of yttrium oxide hydroxide nitrate $Y_4O(OH)_9NO_3$ (JCPDS No. 79-1352), except that some little peaks cannot be finely indexed to monoclinic phase of $Y_4O(OH)_9NO_3$. So, the precursors obtained at pH = 9.0 and pH = 12.0 are presumed to contain the samples with a structural formula of $Lu_4O(OH)_9NO_3$. Additionally, the XRD pattern of the precursors obtained at pH = 12.5 and pH = 13.0 indicated a crystalline phase with good repeatability, but their crystal structures could not be indexed to any known lutetium compounds on the basis of the Joint Committee on Powder Diffraction Standards (JCPDS). On the basis of the EDS results (Fig. S1, ESI†) and the FT-IR spectra (Fig. S2, ESI†), the precursors obtained at pH = 12.5 and pH = 13.0 is presumed to be an inorganic–organic complex compound which constitutes Lu–O, Lu–S, O–H, $–CH_2–$, C=O, C=S and C–N bonds. According to the XRD results, pH value of the reaction solution has a prominent influence on the composition and phase structure of the obtained precursors; also, the solvothermal process at 200 □ did not produce Lu_2O_2S directly.

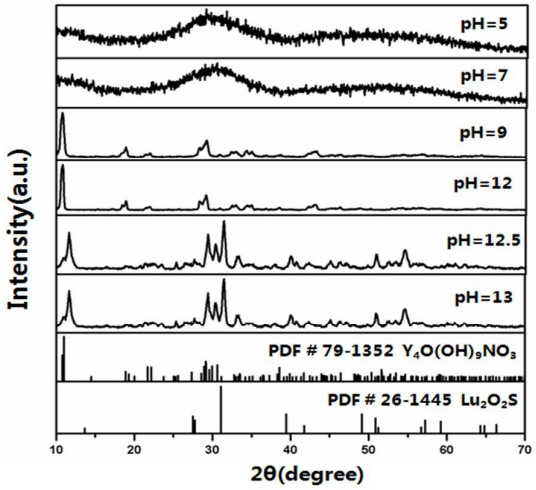

Fig. 2 XRD patterns of precursors obtained at different pH values, and the JCPDS cards No.26-1445 and No.79-1352.

Fig. 3 shows the XRD patterns of the final products as well as the JCPDS card No. 26-1445. When the precursors were annealed at 600 □ for 2 h, the diffraction peaks of all the samples can be satisfactorily indexed to the hexagonal phase of Lu_2O_2S (JCPDS No. 26-1445). No traces of additional peaks from the doped components can be detected, implying that the precursors synthesized at different pH values have all successfully converted into lutetium oxysulfide with high crystallinity. However, it can be observed that the intensities of diffraction peaks are different for varied morphologies. As shown in Fig. 4, the diffraction peaks intensity of the rod-like $Lu_2O_2S:Eu^{3+}$ is the strongest, then flower-like, sphere-like (60-70 nm), cloud-like, nested tetrahedron, and that of the sphere-like (160-170 nm) is the weakest, which means the degree of crystallinity for different morphology is different although they are all obtained at 600 □.

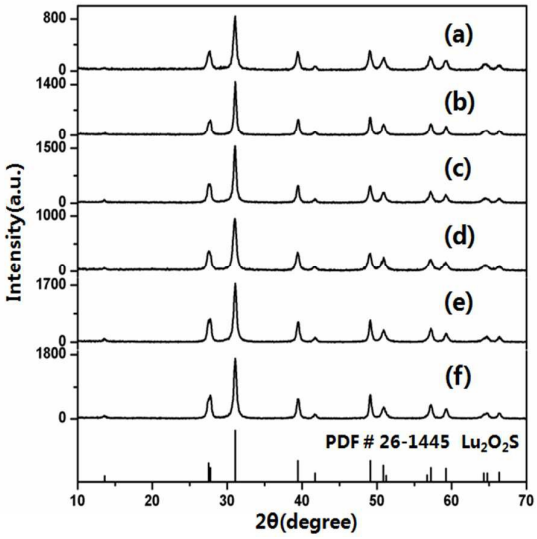

Fig. 3 XRD patterns of annealed products: (a) sphere-like (160-170 nm) at pH = 5, (b) cloud-like at pH = 7, (c) sphere-like (60-70 nm) at pH = 9, (d) nested tetrahedron at pH = 12, (e) flower-like at pH = 12.5, (f) rod-like at pH = 13. Vertical bars denote the standard data for hexagonal phase of Lu_2O_2S (the JCPDS card No.26-1445).

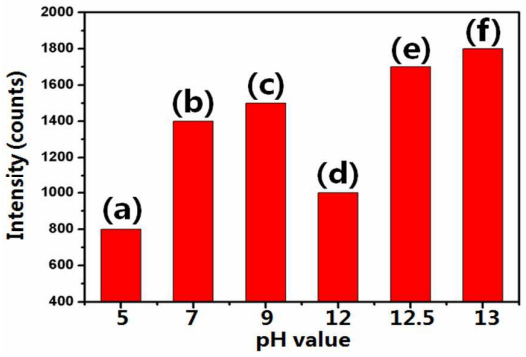

Fig. 4 XRD lines (011) intensity of annealed products: (a) sphere-like (160-170 nm) at pH = 5, (b) cloud-like at pH = 7, (c) sphere-like (60-70 nm) at pH = 9, (d) nested tetrahedron at pH = 12, (e) flower-like at pH = 12.5, (f) rod-like at pH = 13.

The average crystal size of $Lu_2O_2S:Eu^{3+}$ samples was calculated from the Scherrer formula: $D_{hkl}=K\lambda/\beta\cos\vartheta$, D_{hkl} means the size

along the (*h k l*) direction and K is a constant (0.941), where θ and β is the diffraction angle and full-width at half-maximum (FWHM), respectively. The crystallite sizes calculated from diffraction lines (011) and the lattice parameters for various morphologies are listed in table 1. It is seen that the crystallite sizes of all the morphologies are far less than the corresponding particle sizes, indicating that the particles are the assembly of crystallites. It should be noted that the unit cell volumes have changed compared to that of the standard hexagonal phase (JCPDS No. 26-1445), some turned smaller while some turned larger, which might be due to the different doping rites of the Eu^{3+} in different morphology[28]. In addition, the lattice symmetry is also found to change with morphologies, as indicated by the axial ratio of c/a for the present samples, which varied from 1.745 to 1.749 as compared to that of 1.750 for the bulk Lu_2O_2S. It appears that the unique doping sites of Eu^{3+} and lattice symmetry for these morphologies may lead to the unique luminescence properties.

Energy-dispersive spectroscopy (EDS) was performed to determine the composition of the obtained samples. Fig. 5 is the EDS spectra of $Lu_2O_2S:Eu^{3+}$ nanorods, which is similar to those of other morphologies (here is not given). It can be seen that the samples obtained at pH = 5.0, 7.0, 9.0, 12.0, 12.5, and 13.0 all confirm the presence of lutetium (Lu), oxygen (O), sulfur (S), and europium (Eu) elements in $Lu_2O_2S:Eu^{3+}$ micro/nanostructures. No other peaks of impurity elements were detected, indicating that the compound precursors have been converted into $Lu_2O_2S:Eu^{3+}$ completely during the calcination process, which gives further support for the XRD analysis above.

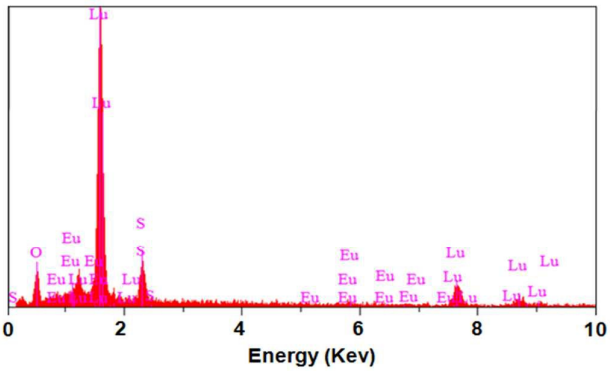

Fig. 5 EDS spectrum of $Lu_2O_2S:Eu^{3+}$ nanorods.

Shown in Fig. 6 are the UV–vis absorption spectra of different morphologies, which are obtained from the diffuse reflectance spectroscopy by the Kubelka-Munk function

$$F(R) = (1-R)^2/2R = K/S$$

Where *R*, *K*, and *S* is the reflection, absorption and the scattering coefficient, respectively. As shown in Fig. 6, all morphologies were nearly transparent in the visible region, while showing an intense band-to-band absorption in the wavelength range below 360 nm.

The value of the optical band gap can be calculated by extrapolating the Kubelka-Munk function to K/S = 0. It is noted that spheres (160-170 nm) and the nested tetrahedron microstructures possessed a similar band-gap E_g around 3.67 and 3.65 eV, which is larger than that of 3.60 eV for the cloud-like, 3.56 eV for the spheres (60-70 nm) and 3.51 eV for the microflowers. Comparatively, the nanorods showed the narrowest band gap of 3.41 eV, which could be related to the lower conduction-band bottom induced by the deep defect energy levels for the highly concentrated defect Lu_2O_2S centres. In addition, the band-gap of Eu^{3+} doped Lu_2O_2S is lower than that of the undoped Lu_2O_2S (3.78 eV), this is due to the chemical defects or vacancies present in the intergranular regions, which forming a new energy level to reduce the band gap energy.

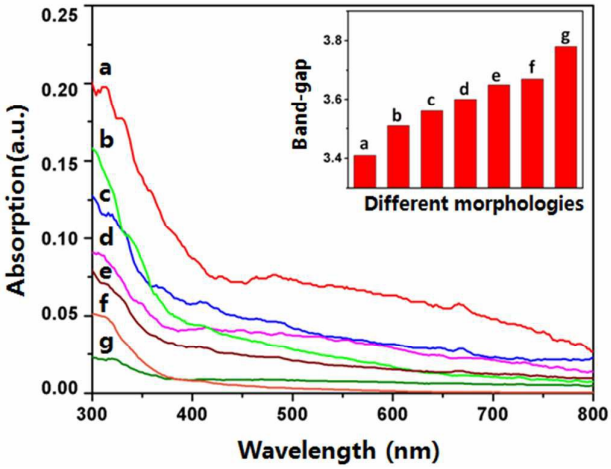

Fig. 6 UV–vis absorption spectra and band- gap energy (inset) of different morphologies: (a) rod-like, (b) flower-like, (c) sphere-like (60-70 nm), (d) cloud-like, (e) nested tetrahedron and (f) sphere-like(160-170 nm), (g) undoped Lu_2O_2S.

Table 1. Cell parameters and crystallite sizes for different morphologies.

Morphologies	Lattice parameters (Å)		c/a	Cell volume ($Å^3$)	Crystallite size（nm）
	a	c			
JCPDS 26-1445	3.707	6.488	1.750	77.20	
Spheres (160-170 nm)	3.713	6.479	1.745	77.37	20.28
Cloud-like	3.708	6.481	1.748	77.19	19.74
Spheres (60-70 nm)	3.709	6.475	1.746	77.18	18.05
Nested tetrahedron	3.707	6.485	1.749	77.23	19.92
Microflowers	3.705	6.478	1.748	77.03	17.99
Nanorods	3.701	6.466	1.747	76.72	17.81

Luminescence properties of $Lu_2O_2S:Eu^{3+}$

Fig. 7 (left) shows the excitation spectra measured in the range 250-450 nm by monitoring the transition $^5D_0$-$^7F_2$ of Eu^{3+} at 626 nm. The excitation spectra consist of a broad band ranging from 250 to 380 nm and weak sharp lines, which are due to the charge transfer band (CTB) of Eu^{3+}– O^{2-}/S^{2-} and the f–f transition of the Eu^{3+} ions, respectively. Herein, it is noted that the rod-like and flower-like showed a strong excitation while sphere-like (60-70 nm), cloud-like and nested tetrahedron microstructures exhibited a similar but weaker excitation intensity. Further, the excitation intensity for the sphere-like (160-170 nm) is the weakest. These observations indicate that the peaks' intensities of the Eu^{3+} ions changed with the micro/nanostructure of their matrix. This may be attributed to the different local environment of the Eu^{3+} in different matrix, since the energy transfers may be associated with it, and it could further modifies the excited levels of the Eu^{3+}.

Fig. 7 (right) shows the emission spectra of different morphologies, all of which have similar photoluminescence (PL) properties. They all contain a group of lines centered at about 539, 555, 582, 586, 594, 615, 626, 653, 686, 696, and 705 nm. They come from the $^5D_2$-$^7F_3$, $^5D_1$-$^7F_1$, $^5D_1$-$^7F_2$ and $^5D_0$-^7F_J (J = 0, 1, 2, 3, and 4) transitions of the Eu^{3+} ions. The strongest red emission at 626 nm arises from the forced electric-dipole $^5D_0$-$^7F_2$ transitions of the Eu^{3+} ions. Furthermore, from Fig. 7, it can be found that the morphologies of obtained samples have an important effect on their luminescent intensity. The nanorods (Fig. 7f) exhibit the strongest PL intensity, the spheres (160-170 nm, Fig. 7a) exhibit the weakest, the flower-like structures (Fig. 7e), spheres (60-70 nm, Fig. 7c), nested tetrahedron microstructures (Fig. 7d) and cloud-like structures (Fig. 7b) are in between.

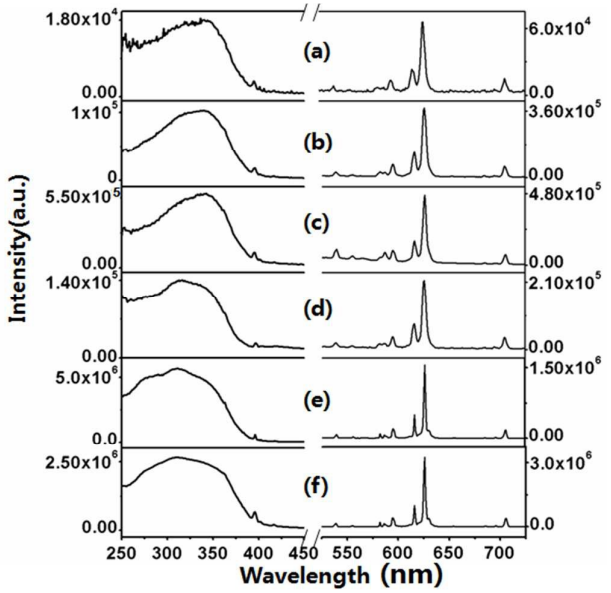

Fig. 7 Photoluminescence excitation and emission spectra for different morphologies: (a) sphere-like (160-170 nm), (b) cloud-like, (c) sphere-like (60-70 nm), (d) nested tetrahedron, (e) flower-like and (f) rod-like.

The different PL intensity can be interpreted from following aspects. First, the PL intensity is related to the degree of crystallinity. As is well known, the higher degree of crystallinity for the sample, the fewer defects it has, which indicate the decrease of non-radiative radiations as well as the luminescence quenching, and will be helpful to enhance the PL performance[29, 30]. As discussed above (Fig. 4), the degree of crystallinity for different morphologies in the descending order are rod-like, flower-like, sphere-like (60-70 nm), cloud-like, nested tetrahedron and sphere-like (160-170 nm) structures, which is in consistent with the luminescence intensity. Second, the PL intensity is related to the band gap energy for different morphologies. Combined with Fig. 6 and Fig. 7, it can be seen that the PL intensity increased with the decrease of band gap energy. Obviously, the high band gap energy makes the transition of the electron difficult, so the decrease of the band gap energy makes the transition of $^5D_0$–$^7F_2$ easier and red emission enhanced. Third, the stronger emission intensity also may be caused by asymmetry of the crystal fields around Eu^{3+}. It is well known that the relative intensity for emission transition $^5D_0$–$^7F_2$ to $^5D_0$–$^7F_1$ robustly depends on the local symmetry of Eu^{3+}, so the ratio I_{02}/I_{01} = area ($^5D_0$–$^7F_2$)/area ($^5D_0$–$^7F_1$) can be used to obtain some structural information about the luminescence centres[31-33]. As shown in Fig 8, the ratios I_{02}/I_{01} of the ($^5D_0$–$^7F_2$) and ($^5D_0$–$^7F_1$) integrated transition intensities are determined to be 9.214 for the nanorods, 8.718 for the microflowers, 7.815 for the nanospheres (60-70 nm), 7.356 for the cloud-like nanostructures, 7.350 for the nested tetrahedron microstructures and 6.276 for the nanospheres (160-170 nm). Always, the increase in the ratio I_{02}/I_{01} denotes a decrease in local symmetry and an increase in the covalence of Eu^{3+}-O^{2-} bonding[32]. It is noted that the luminescent intensity increased with the decrease in the crystal field symmetry around Eu^{3+}[34]. Therefore, asymmetry of the crystal fields around Eu^{3+} is responsible for the enhancement of red emission. As a result, the PL intensity could be arranged as a function of morphologies: rod-like > flower-like > sphere-like (60-70 nm) > cloud-like > nested tetrahedron > sphere-like (160-170 nm).

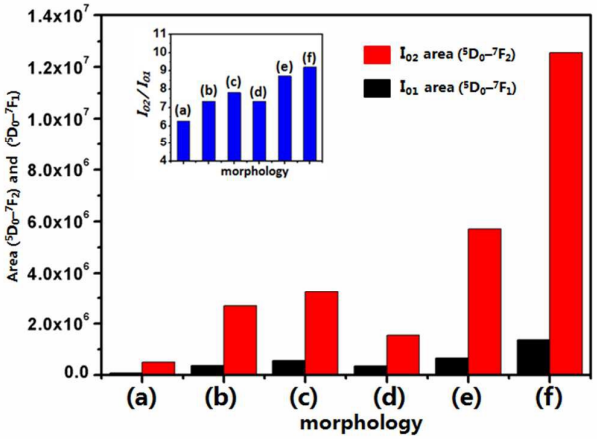

Fig. 8 Area ($^5D_0$–$^7F_2$), area ($^5D_0$–$^7F_1$) and I_{02}/I_{01} (inset) for the different morphologies: (a) sphere-like (160-170 nm), (b) cloud-like, (c) sphere-like (60-70 nm), (d) nested tetrahedron, (e) flower-like and (f) rod-like.

The effective lifetimes for different morphologies of the $Lu_2O_2S:Eu^{3+}$ micro/nanostructures were further investigated. Shown in Fig. 9 is a decay curve of the Eu^{3+} (λ_{ex}= 270 nm and λ_{em}= 626 nm) in the Lu_2O_2S nanorods depicted in a logarithmic intensity. This decay curve cannot be fitted in terms of a single-exponential function, but is reproduced well by a double-exponential function,

$$I_t=A_1exp(-t/\tau_1)+A_2exp(-t/\tau_2),$$

Where τ_1 and τ_2 are the long and short components of the luminescence lifetimes, and A_1 and A_2 are the fitting parameters, respectively. The effective lifetime is defined as,

$$[\tau]=(A_1\tau_1^2+A_2\tau_2^2)/(A_1\tau_1+A_2\tau_2).$$

The effective lifetimes for different morphologies were calculated. The nanorods' average lifetime is 0.998 ms which is higher than that of microflowers 0.876 ms, nanospheres (60-70 nm) 0.726 ms, cloud-like nanostructures 0.698 ms, nested tetrahedron microstructures 0.573 ms and nanospheres (160-170 nm) 0.469 ms. It is noted that the tendency of the lifetime is in correspondence with that of the PL intensity. Namely, the effective lifetimes are also strongly dependent on the morphologies, which may be closely related to the lattice defects and band gap energy pertinent to the special morphologies[35]. In general, decay kinetics behavior depends on the number of luminescent centers, energy transfer and defects in the host[34, 36]. So, the longest lifetime of the nanorods may be mainly attributed to the decrease in nonradiative transition rate caused by surface defects in nanocrystals.

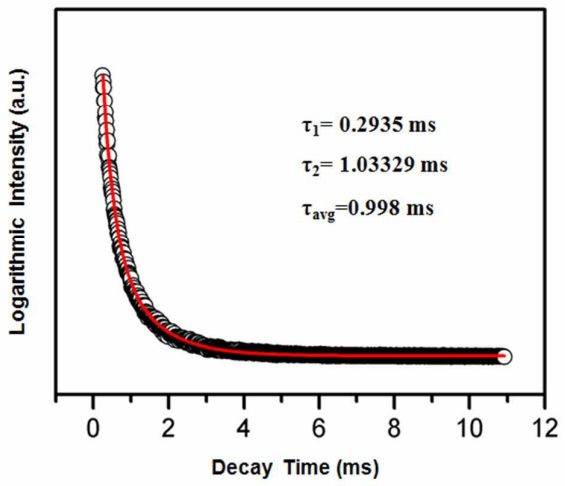

Fig. 9 Photoluminescence decay curve of the $Lu_2O_2S:Eu^{3+}$ for the nanorods

Possible growth mechanism of as-prepared $Lu_2O_2S:Eu^{3+}$ precursors

As mentioned above, the pH value is the most important controlling factor in the course of the morphology change of the as-prepared $Lu_2O_2S:Eu^{3+}$ nanostructured materials. To explain the effect of pH value on the change of the morphology, a schematic illustration displayed the possible formation mechanism of the various morphologies under different pH values as shown in Fig. 10.

Obviously, the formation process of the different morphologies can be explained by a so-called two-stage growth process, which include dissolution–recrystallization[37] and self-assembly[38]. As indicated by the SEM images in Fig. 1 and the crystallite sizes listed in Table 1, the size of the samples is much larger than the crystallite size that calculated by XRD, which demonstrated that the different morphologies are an assembly of tiny nanoparticles, which means that the growth of larger crystals occurs based on the integration and assembly of small crystals. In the first stage, a fast nucleation of the nuclei in solution formed amorphous primary particles. In the second stage, the primary particles crystallized, followed by aggregation and anisotropic or isotropic growth to form diverse morphologies.

When the pH value of the solution is adjusted to 5.0, there may exist a strong repulsion between the contacting surfaces among the primary particles due to the relatively high concentration of free H^+ ions in solution. The primary particles can be well-proportioned adsorbed on different crystal facets of the growing particles because of the strong repulsion. Thus, the isotropy grown of the primary particles leads to the formation of nanospheres.

When the pH value is adjusted to 7.0, the solution is electrically neutral, so the repulsion between each primary particles become weakened, the slight alteration of the electrostatic attraction in aqueous solution might be a sensitive factor in deciding the anisotropic growth of the primary particles and leads to the formation of the cloud-like nanostructure.

When the pH value is adjusted to 9.0, the concentration of OH^- ions in the reaction solution becomes slightly higher than that of H^+ ions. The repulsion and attraction between each primary particle achieved a balance, so the isotropic crystal growth becomes the predominant growth behaviour and the driving force for the isotropic growth of the precursors may derive from the decrease of the surface energy and the chemical potential in solution. Therefore, nanospheres were formed by the self-assembly of the primary particles.

When the pH value is increased to 12.0, the concentration of OH^- ions is far above that of the H^+ ions, which leads to the following secondary anisotropic growth stage. Always the growth rate of a crystal face is determined by the relative specific energy of each face, and the fastest crystal growth will occur in the direction perpendicular to the face with the highest surface energy, resulting in the fast growing planes with high energy disappearing to leave behind the slowest growing planes with low energy[39]. So the anisotropic crystal growth leads to the formation of the nested tetrahedron microstructures.

When the pH value was increased to 12.5, there will be a higher chemical potential in solution, which is preferable for the anisotropic growth. In the first stage, the nanoparticles were formed and fused with each other to grow into the pristine nanorods through the dissolution/crystallization process. At the same time, under high pressure treatment and solution charge potential drive, the nanorods attach to each other in an oriented fashion to reduce the surface energy of the system and finally, these nanorods self-assembled into nano-bundles. As a result, these assembled nanorods are constructed into ordered microflowers.

When the pH value is increased to 13.0, implies a higher OH^- ions concentration in solution, which is high enough to lead to the electrostatic repulsion between the primary particles. So the nucleation of the precursors were accelerated and the anisotropic crystal growth becomes the predominant growth behaviour, the fastest crystal growth will occur in one direction which leads to the formation of the nanorods.

In fact, the mechanism for the formation of the multiform morphologies is very complicated because of several factors, including crystal face attraction, electrostatic and dipolar fields associated with the aggregate, van der Waals forces, hydrophobic interactions, and hydrogen bonds. Further work is necessary to uncover these effects on the self-assembly processes and the formation of many other novel morphologies.

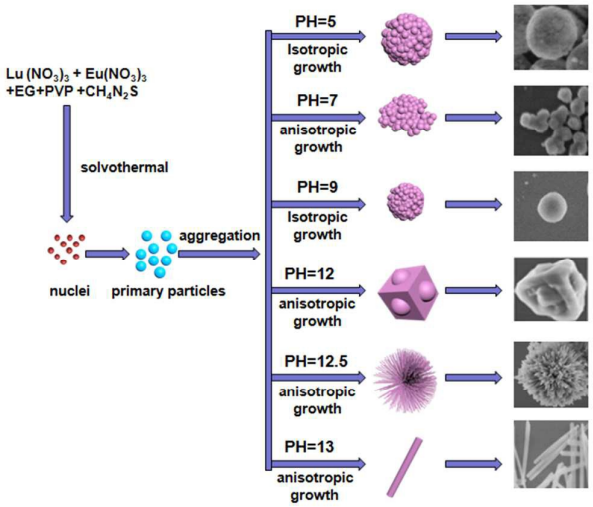

Fig. 10 Formation schematic of $Lu_2O_2S:Eu^{3+}$ micro/nanostructured materials with various morphologies under the different pH values.

Conclusions

In summary, three-dimensional (sphere-like, cloud-like, nested tetrahedron, and flower-like) and one-dimensional (rod-like) $Lu_2O_2S:Eu^{3+}$ micro/nano-structures have been successfully achieved by a facile solvothermal method combining with a post-calcining process. It is found that the pH value of the initial reaction solution plays a key role in controlling the morphologies of the final products. Moreover, we not only analyze the possible mechanisms for the diverse morphologies, but also expound the morphology-dependent red luminescence property. The ability to generate $Lu_2O_2S:Eu^{3+}$ micro/nanostructures with diverse morphologies and photoluminescence properties provides a great opportunity for systematically tailoring the red luminescence for a broad class of technological applications.

Acknowledgements

This work is financially supported by the National Natural Science Foundation of China (Grant Nos. 21171066 and 51272085), the Openning Research Funds Projects of the State Key Laboratory of Inorganic Synthesis and Preparative (2016–06), and the Key Technology and Equipment of Efficient Utilization of Oil Shale Resources, No. OSR-05.

Notes and references

1. Y. T. Chang, H. L. Chang, K. W. Su and Y. F. Chen, *Optics Express*, 2009, **17**, 11892-11897.
2. L. Chen, K. J. Chen, S. F. Hu and R. S. Liu, *Journal of Materials Chemistry*, 2011, **21**, 3677-3685.
3. Q. Y. Zhou, A. G. Tian, H. F. Zou, Z. M. Xie, G. Lei, J. Huang, C. M. Wang, H. W. Wang, J. S. Zhang and S. Y. Chen, *Plant Biotechnology Journal*, 2008, **6**, 486-503.
4. S. Jie, S. Ling-Dong, Z. Jia-Dan, W. Liu-He, S. Hong-Fang and Y. Chun-Hua, *Advanced Functional Materials*, 2010, **20**, 3708-3714.
5. F. Wang and X. Liu, *Chem.soc.rev*, 2009, **38**, 976-989.
6. W. Feng, H. Yu, L. Chin Seong, L. Yunhao, W. Juan, X. Jun, C. Hongyu, Z. Chun, H. Minghui and L. Xiaogang, *Nature*, 2010, **463**, 1061-1065.
7. H. B. Wang, L. J. Ou, K. J. Huang, X. G. Wen, L. L. Wang and Y. M. Liu, *Canadian Journal of Chemistry*, 2013, **91**, 1266-1271.
8. X. Sun, G. Zhang, M. Cai, S. Sun and R. Li, US, 2011.
9. S. Erdei, *Journal of Materials Science*, 1995, **30**, 4950-4959.
10. F. Wang, X. Chen, D. Liu, B. Yang and Y. Dai, *Journal of Molecular Structure*, 2012, **1020**, 153–159.
11. Y. Song, H. You, Y. Huang, M. Yang, Y. Zheng, L. Zhang and N. Guo, *Inorganic Chemistry*, 2010, **49**, 11499-11504.
12. Q. Dai, H. Song, M. Wang, X. Bai, B. Dong, R. Qin, X. Qu and H. Zhang, *Journal of Physical Chemistry C*, 2008, **112**, 19399-19404.
13. S. H. Jung, E. Oh, H. Lim, D. S. Shim, S. Cho, K. H. Lee and S. H. Jeong, *Crystal Growth & Design*, 2009, **9**, 3544-3547.
14. W. Zhang, #x, Xiong, M. Nishiura and Z. Hou, *Chemistry - A European Journal*, 2007, **13**, 4037–4051.
15. H. Qiao, Y. C. Jia, Y. H. Zheng, N. Guo, Q. Zhao, W. Z. Lv and H. P. You, *Crystengcomm*, 2012, **14**, 5830-5835.
16. Y. Li, J. Wang, Z. Yong, M. N. Banis, L. Jian, D. Geng, R. Li and X. Sun, *J Colloid Interface Sci*, 2012, **369**, 123–128.
17. S. Huang, X. Zhang, L. Wang, L. Bai, J. Xu, C. Li and P. Yang, *Dalton Trans*, 2012, **41**, 5634-5642.
18. J. J. Dipl.-Chem., P. W. Roesky Dr., N. Ajellal, S. M. Guillaume, N. Susperregui and L. Maron Dr., *Chemistry (Weinheim an der Bergstrasse, Germany)*, 2010, **16**, 4629–4638.
19. S. Yanhua, Y. Hongpeng, H. Yeju, Y. Mei, Z. Yuhua, Z. Lihui and G. Ning, *Inorganic Chemistry*, 2010, **49**, 11499-11504.
20. M. Hao-Xin, Z. Ya-Wen, S. Rui, Y. Zheng-Guang, S. Ling-Dong, Y. Li-Ping and Y. Chun-Hua, *Journal of the American Chemical Society*, 2006, **128**, 6426-6436.
21. Z. Qi, Y. Zheng, G. Ning, Y. Jia, Q. Hui, W. Lv and H. You, *Crystengcomm*, 2012, **14**, 6659-6664.
22. G. Wang, H. Zou, H. Zhang, L. Gong, Z. Shi, X. Xu and Y. Sheng, *Materials Letters*, 2014, **128**, 256–258.
23. G. Wang, H. Zou, B. Zhang, Y. Sun, Q. Huo, X. Xu and B. Zhou, *Optical Materials*, 2015, **45**, 131–135.
24. B. Clemens, C. Xiaobo, N. Radha and E.-S. Mostafa A, *Chemical Reviews*, 2005, **105**, págs. 1025-1102.
25. L. Zhang, H. Yang, J. Yu, F. Shao, L. Li, F. Zhang and H. Zhao, *J.phys.chem.c*, 2009, **113**, 5434-5443.
26. W. Jiwei and P. A. Tanner, *Journal of the American Chemical*

Society, 2009, **132**, 947-949.
27. F. Bonnet, M. Visseaux, D. Barbier-Baudry, E. Vigier and M. M. Kubicki, *Chemistry*, 2004, **10**, 2428–2434.
28. C. Daqin and W. Yuansheng, *Nanoscale*, 2013, **5**, 4621-4637.
29. L. Yang, L. Li, M. Zhao and G. Li, *Physical Chemistry Chemical Physics Pccp*, 2012, **14**, 9956-9965.
30. C. Feller, E. Schouller, F. Thomas, J. Rouiller and A. J. Herbillon, *Soil Science*, 1992, **153**, 293-299.
31. L. Yang, G. Li, M. Zhao, J. Zheng, X. Guan and L. Li, *Crystengcomm*, 2012, **14**, 3227-3235.
32. R. Han, R. Hu and K. Chen, *Optical Materials*, 2009, **32**, 329–333.
33. S. Ray, A. Banerjee and P. Pramanik, *Materials Science\s&\sengineering：b*, 2009, **156**, 10–17.
34. L. Yang, G. Li, M. Zhao, X. Guan, L. Li and J. Zheng, *Crystengcomm*, 2012, **14**, 3227-3235.
35. L. Yang, G. Li, M. Zhao, J. Zheng, X. Guan and L. Li, *Nanotechnology*, 2012, **23**, 245602-245610(245609).
36. M. Xu, L. Wang, D. Jia and H. Zhao, *Phys.chem.chem.phys*, 2015.
37. Y. Wang, M. Lin and A. Tuel, *Microporous & Mesoporous Materials*, 2007, **102**, 80–85.
38. W. Gregory J, M. Aaron S, M. David R G, S. Jamie C and W. Geoffrey D, *Langmuir*, 2006, **22**, 2016-2027.
39. L. Fang, Y. Bing, C. Hao Hong and Z. Jing Tai, *Inorganic Chemistry*, 2009, **48**, 7576-7584.
40. J. Tang and A. P. Alivisatos, *Nano Letters*, 2006, **6**, 2701-2706.

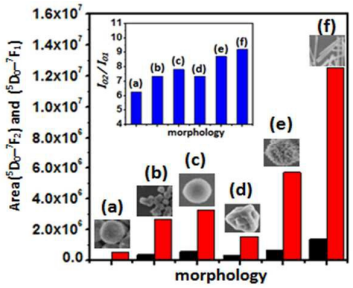

The dependence of $Lu_2O_2S:Eu^{3+}$ luminescence performance on different morphologies has been explored and the possible reasons are proposed.